7th AIAA/CEAS Aeroacoustics Conference
28-30 May 2001 Maastricht, Netherlands

A01-30936

AIAA 2001-2226

Computation of the noise radiated by a subsonic cavity using direct simulation and acoustic analogy *

Xavier Gloerfelt[†], Christophe Bailly[‡] and Daniel Juvé[§]

Laboratoire de Mécanique des Fluides et d'Acoustique
Ecole Centrale de Lyon & UMR CNRS 5509
BP 163, 69131 Ecully cedex, France.

Abstract

The goal of this paper is to investigate the acoustic field generated by the flow over a cavity using two different and complementary numerical methods. First, a Direct Numerical Simulation (DNS) of the 2-D compressible Navier-Stokes equations is performed to obtain directly the acoustic field. Second, this reference solution is compared to solutions provided by hybrid methods using the flowfield computed inside the cavity combined with an integral formulation to evaluate the far-field noise. Two integral methods are studied: the acoustic analogy of Ffowcs Williams and Hawkings (FW-H) and a wave extrapolation method based on FW-H equation. Both show a good agreement with DNS but the first one is more expensive owing to an additional volume integral. The extrapolation method from a surface is more efficient and provide a complementary tool to extend CAA near-field to very far field. These methods help the analysis of wave patterns, by separating the direct waves from the reflected ones.

1. Introduction

The computation of flow noise is a challenging problem insofar as there are large disparities between fluctuations in the flow and in the sound field. Energy radiated through the acoustic farfield is indeed smaller than the one of the aerodynamic nearfield by $\mathcal{O}(M^4)$, and the involved length scales are very different between the eddy scale and the acoustic wavelength. The propagative nature of sound differs also greatly from the vortical behaviour of the flow. That's why approaches specific to aeroacoustics have been developed. The first group of approaches separates the aerodynamic calculation and the noise propagation problem in order to apply at each step the most appropriate method. Basic difficulties in these so-called *hybrid methods* are the modelling of the source terms from aerodynamic fluctuations and the ability of the wave operator to include complex acoustic-flow interactions. One of the first theories on aerodynamic noise generation was given by the acoustic analogy of Lighthill.[1] It was extended by Ffowcs Williams and Hawkings[2] (FW-H) to take the effects of solid boundaries into account. This powerful analytical tool can be used in connection with numerical methods to evaluate noise radiation. Another relevant issue is the use of a surface integral formulation, like Kirchhoff's or porous FW-H methods, for prediction of the acoustic field. These two approaches have similar analytical insights based on Green function formalism and suffer both from the limitation of the observer in a uniform flow. Linearized Euler Equations (LEE) can provide a more complete propagation operator for acoustics in non-uniform media. The coupling of these equations with a Navier-Stokes equations solver was demonstrated by Freund[3] but offers only poor gain compared to direct calculation. Bailly *et al.*[4] have introduced source terms in LEE with success for different free shear flows. The main difficulty is the modelling of the source terms in more complex configurations. We propose here to study numerical issues of two integral formulations: the Ffowcs Williams-Hawkings analogy and a wave extrapolation method (WEM) from a surface, sometimes called the porous FW-H integral method. However these two hybrid approaches do not account for the aerodynamic-acoustic coupling and they lack the modelling of the non-uniform flow effects.

[†]Ph. D. Candidate
[‡]Assistant Professor, Member AIAA
[§]Professor, Member AIAA

Turning to account the fact that both fluctuations are solutions of compressible Navier-Stokes equations, it is possible to obtain acoustic and aerodynamic fields in the same calculation. However, owing to the great disparities between these two quantities, in classical CFD (Computational Fluid Dynamics), acoustics is either not resolved accurately or not resolved because of the numerical schemes used and inadequate grid cell size or time step. Moreover, reflections due to the boundary conditions can shade the physical acoustic wave field. That's why specific algorithms and appropriate boundary conditions have been developed. We then talk about CAA (Computational AeroAcoustics). The CAA codes essentially rest upon high order explicit schemes minimizing dispersion and dissipation of acoustic waves. These choices are numerically expensive but it is the price to make the aerodynamic flow and the acoustic field coexist. CAA has already been able to reproduce sound radiation from free flows like a 3-D round jet[5] with qualitatively and quantitatively good agreement with experimental data.

In this paper we focus our attention to impinging shear layer, which gives rise to intense coherent oscillations as well as associated noise radiation in a wide range of applications.[6] The chosen test case is a 2-D rectangular cavity, as well for its geometrical simplicity as for its relevance to many practical concerns. However, geometrical simplicity does not imply flow simplicity, and cavity flows provide an assortment of interesting theoretical questions and experimental observations. The cavity flow, characterized by a severe acoustic environment within and outside the cavity, arises from a feedback loop, locked in by the geometry and the flow characteristics. Despite numerous prior investigations, there remain some central questions which must be adressed if an understanding of the self-sustained mechanism is to be achieved. We hope that aeroacoustic simulations can provide a new tool to investigate how the deformation of flow structures, their interactions with the upstream edge, the dynamic of the separated shear layer, the internal recirculating flow or the changes of flow regime with changing geometry and flow parameters are related to the intense radiated noise.

The aim of this paper is to study two integral hybrid methods with direct computation as reference and to evaluate their practical interest and complementarity. In particular, for the case of cavity flow it is shown how these different tools can help us to analyse the radiated acoustic field. In the first part of this paper, we shall present the direct computation of Navier-Stokes equations for a two-dimensional rectangular cavity with aspect ratio of 2, paying particular attention to the comparison between these numerical results and Krishnamurty's experiments.[7] In the second part, we shall describe the two integral methods based on FW-H equation and compare the results to the DNS. We shall show how these simulations can help the understanding of the nature of the acoustic radiations.

2. Direct computation of cavity noise

2.1 Introduction

Despite the amount of numerical studies published on cavity flows, few deal with radiated noise. Initial attemps have been made in supersonic cases. These first CFD computations of compressible cavity flows used the two dimensional unsteady RANS (Reynolds Averaged Navier-Stokes) equations with a turbulence model.[8] The effectiveness of such models for separated flows remains an open question. Slimon[9] *et al.* have found that RANS simulations show a strong sensitivity to the choice of turbulence models. Tam *et al.*[10] showed that the results are affected by high values taken by the turbulent viscosity. They even noticed better results for the estimation of the time-averaged surface pressure field with a zero-equation turbulence model. That's why Rona and Dieudonné[11] preferred to study laminar flow motion. The absence of an eddy viscosity and a second-order algorithm give a moderate dispersion and dissipation. However, this choice, as well as the one of a relaxation length, is often made on an *ad-hoc* basis. To compute the broadband nature of cavity noise at high Reynolds numbers, it is important to take account of the turbulent mixing. Zhang[12] developed an approach coupling the unsteady RANS equations and a $k-\omega$ model including compressibility corrections. But all these applications were performed with supersonic flows, simplifying the problem.

The first computations of acoustic radiation from a cavity with a subsonic grazing flow have been carried out recently by Colonius[13] *et al.*, and Shieh & Morris[14] using 2-D Direct Numerical Simulation (DNS) at a Reynolds number based on cavity depth $\mathrm{Re}_D \simeq 5000$. These simulations show a transition to a new flow regime when the ratio L/δ_θ of the cavity length over the momentum thickness becomes large. This mode is characterized by the shedding of a single vortex which occupies all the cavity. The periodic ejection of this structure is associated with an increase of the cavity drag. A similar transition was noted in the experiments of Gharib & Roshko[15] in a water tunnel. The new regime was called wake mode because of the drag increase. However, the presence of the wake mode has not been seen in experiments of compressible cavity flows at subsonic speeds. The same numerical bifurcation has also been noted by the authors.[16] Does it result from the very low Reynolds numbers imposed by DNS or from the two-dimensional approach? To investigate higher Reynolds numbers ($\mathrm{Re}_D \simeq 2 \times 10^5$), Shieh & Morris[17] applied CAA tools to solve unsteady RANS with a turbulence model: the one equation Spalart-Allmaras turbulence model and Detached Eddy Simulation have been implemented. The transition to a wake mode is still observed, indicating that it could be related to the 2-D behaviour rather than to the Reynolds number. When the cavity length is large compared to the thickness of the incoming boundary layer, Najm & Ghoniem[18] show in the same manner that the recirculation zone takes the form of a large-scale eddy that breaks away and migrates downstream, overshadowing the role of the usual smaller-scale vortices. However, this too strong recirculating flow is fed by the two-dimensional inverse cascade of energy. Vortex stretching, necessarily 3-D, should modify significantly the turbulent mixing between the clipped part of the shear layer and the corresponding counter-rotating vortex produced by the conservation of vorticity at the downstream edge. This turbulent mixing would prevent untimely transition to wake mode. In our 2-D simulation, a short aspect ratio and a relatively thick incoming boundary layer are chosen to ensure the shear layer mode of oscillations.

We try to reproduce numerically Krishnamurty's experiment[7] with the same dimensions as in the experiment. The latter studied the acoustic radiation from two-dimensional rectangular cavities cut into a flat surface at low Reynolds numbers. The acoustic fields were investigated by means of Schlieren observations, interferometry, and hot-wire anemometer. The measurement used a cutout spanning the 4 by 10 inch transonic wind tunnel and ending by a moving plate to obtain cavities of various length L, the depth D being the same for all of them, fixed at 0.1 inch. We present here the simulation of the case where the length-to-depth ratio is 2 ($L = 5.18$ mm and $D = 2.54$ mm) where the boundary layer ahead of the cavity is laminar and the freestream Mach number is 0.7. The Reynolds number based on cavity depth is $\mathrm{Re}_D = 41000$. The choice of a high subsonic speed is interesting because the frequency increases slightly with Mach number and the cavity is no more compact relatively to the acoustic wavelength. Moreover, the test case is more relevant for integral methods because mean flow effects on sound propagation become important.

2.2 Numerical methods

Governing equations

A Direct Numerical Simulation (no model) of the 2-D compressible Navier-Stokes equations is performed. The conservative form of these equations in a Cartesian coordinate system can be written as:

$$\frac{\partial \mathbf{U}}{\partial t} + \frac{\partial \mathbf{E_e}}{\partial x_1} + \frac{\partial \mathbf{F_e}}{\partial x_2} - \frac{\partial \mathbf{E_v}}{\partial x_1} - \frac{\partial \mathbf{F_v}}{\partial x_2} = 0$$

where:

$$\begin{aligned}
\mathbf{U} &= (\rho, \rho u_1, \rho u_2, \rho e)^t \\
\mathbf{E_e} &= (\rho u_1, p + \rho u_1^2, \rho u_1 u_2, \rho u_1 h)^t \\
\mathbf{F_e} &= (\rho u_2, \rho u_2 u_1, p + \rho u_2^2, \rho u_2 h)^t \\
\mathbf{E_v} &= (0, \tau_{11}, \tau_{12}, u_1\tau_{11} + u_2\tau_{12} + q_1)^t \\
\mathbf{F_v} &= (0, \tau_{21}, \tau_{22}, u_1\tau_{21} + u_2\tau_{22} + q_2)^t
\end{aligned}$$

The quantities ρ, p, u_i are the density, pressure, and velocity components, while e and h are the total energy and total enthalpy per mass unit. For a perfect gas,

$$\begin{aligned}
e &= p/[(\gamma - 1)\rho] + (u_1^2 + u_2^2)/2 \\
h &= e + p/\rho \\
p &= r\rho T
\end{aligned}$$

where T is the temperature, r the gas constant, and γ the ratio of specific heats. The viscous stress tensor τ_{ij} is modelled as a Newtonian fluid and the heat flux component q_i models thermal conduction in the flow with Fourier's law:

$$\begin{aligned}
\tau_{ij} &= \mu \left(\frac{\partial u_i}{\partial x_j} + \frac{\partial u_j}{\partial x_i} - \frac{2}{3}\delta_{ij}\frac{\partial u_k}{\partial x_k} \right) \\
q_i &= \frac{\mu c_p}{\sigma}\frac{\partial T}{\partial x_i}
\end{aligned}$$

where μ is the dynamic molecular viscosity, σ the Prandtl number, and c_p the specific heat at constant pressure.

Algorithm

When the above equations are solved numerically, it is imperative that, as the frequency is varied, neither the wave amplitude nor its propagation speed be altered by the numerical scheme. That's why, following the work of Bogey,[19] high order algorithms are implemented. The equations are advanced in time using an explicit 4th order Runge-Kutta scheme.

The Dispersion-Relation-Preserving scheme developed by Tam and Webb[20] is used to obtain spatial derivatives. A selective damping has also to be introduced in order to filter out non physical short waves resulting from the use of finite differences and/or treatment of boundary conditions.

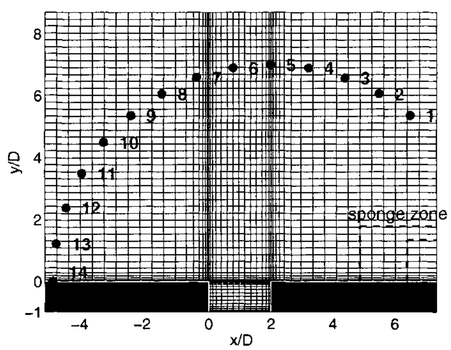

Figure 1: Computational grid for cavity $L/D = 2$ (shown every other ten points). •: data sampling locations for directivity evaluation. (— — —): location of the progressive additional sponge zone.

Boundary treatment

This is the second key point of an aeroacoustic simulation. We need nonreflecting conditions to avoid spurious reflections which can superpose to physical waves. To this end, the radiation boundary conditions of Tam and Dong,[21] using a polar asymptotic solution of the linearized Euler equations in the acoustic far-field, is applied to the inflow and upper boundaries. At the outflow, we combine the outflow boundary conditions of Tam and Dong, where the asymptotic solution is modified to allow the exit of vortical and entropic disturbances, with a sponge zone to dissipate vortical structures in the region where the shear layer leaves the computational domain. This sponge zone, represented in figure 1, uses grid stretching and progressive additional damping terms. Bogey *et al.*[22] have shown its efficiency in situations where large amplitude non linear disturbances must exit the domain without significant numerical reflections.

Along the solid walls, the nonslip condition applies. The wall temperature T_w is calculated using the adiabatic condition. We keep centered differencing at the wall to ensure sufficient robustness using ghost points. This overspecification at the wall can generate spurious high-frequency waves which are eliminated by artificial damping.

Numerical specifications

The computational mesh, displayed in figure 1, is built up from nonuniform Cartesian grid with 147×161 points inside the cavity and 501×440 outside, highly clustered near the walls. The minimum step size corresponds to $\Delta y^+_{min} = 0.8$ in order to resolve the viscous sublayer. The computational domain extends over $8.5D$ vertically and $12D$ horizontally to include a portion of the radiated field. The upstream and downstream boundaries are sufficiently far away from the cavity to avoid possible self-forcing. The spacing between two points reaches a value $\Delta y_{max} = 2.9 \times 10^{-5}$ m in the cavity and $\Delta y_{max} = 5.6 \times 10^{-5}$ m in the acoustic region.

The initial condition is a polynomial expression of the laminar Blasius boundary layer profile for a flow at Mach 0.7. The initial boundary layer thickness at the cavity leading edge is $\delta_0 \approx 0.2D$; it corresponds to a ratio $L/\delta_\theta \approx 50$, where L is the cavity length and δ_θ the momentum thickness. The freestream air temperature T_∞ is 298.15 K and the static pressure p_∞ is taken as 1 atm.

Owing to the strong anisotropic computational mesh, we have a very stiff discretized system. For explicit time marching schemes, an extremely small time step has to be used in order to satisfy the stability CFL criterion: $\Delta t = 0.7 \times \Delta y_{min}/c_\infty = 6.06 \times 10^{-9}$ s. The mesh Reynolds number of the selective damping is chosen as $R_S = 4.5$. This artificial dissipation is applied a second time near the walls and especially near the two edges.

The computation is 4 hours long on a Nec SX-5, with a CPU time of 0.4 μs per grid point and per iteration.

2.3 Results and discussion

Far-field results

Figure 2 gives a monitored pressure history at $x/D = -0.04$ et $y/D = 2D$ in the beginning of the acoustic region. The flow reaches a self-sustained oscillatory state after a time of about $25D/U_\infty$ but is still irregular until $65D/U_\infty$. During the first period, the natural cavity modes grow in amplitude and saturate. Then transient is going on during the time needed by the recirculating flow to get installed in the cavity.

The corresponding sound pressure level spectrum

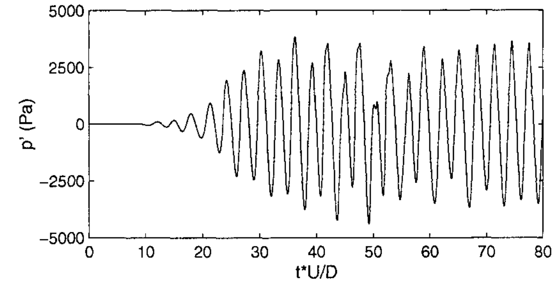

Figure 2: Pressure history versus time at $x/D = -0.04$ and $y/D = 2D$.

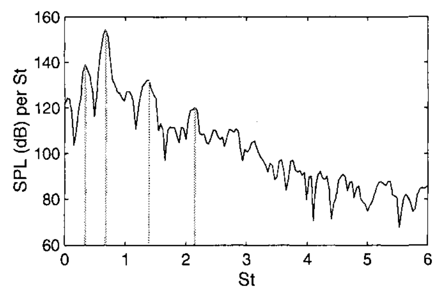

Figure 3: Spectrum of pressure fluctuations at $x/D = -0.04$ and $y/D = 2D$ versus the Strouhal number St$= fL/U_\infty$.

is depicted in figure 3. It displays one principal peak at St= 0.68, which corresponds to the periodic impingement of coherent structures at frequency β. Several secondary peaks are observable. The peaks at St= 1.39 and St= 2.14 are the first 2β and second 3β harmonics of principal frequency β. The low-frequency component at $\beta/2$ (St= 0.38) can be associated with a low-frequency modulation by the recirculating zone, which alters periodically the average trajectory of the incident vortex. Most of the noise energy is concentrated at the resonant frequency and its first harmonics. A Schlieren visualization, corresponding with vertical gradients of density, shows the structure of the radiated field in figure 4(a). Two wave patterns are visible for the positive gradients (dark), which interfer during propagation. Their strong upstream directivity is characteristic of high speed convection by the free stream. These radiations are in qualitatively good agreement with the Schlieren picture of Krishnamurty (fig. 4(b)). The experimental Strouhal number of oscillations is St= 0.71, corresponding to an error of 5% on the frequency β found in our simulation. The Rossiter semi-empirical formula[23] provides St= 0.71 for this configuration with always two vortices in the shear layer.

Krishnamurty[7] measured the intensity of acoustic radiation through interferometry. He found that the acoustic field could be very intense with values greater than 163 dB. These high intensity levels are also found in the present simulation, with a magnitude of sound pressure levels about 160 dB.

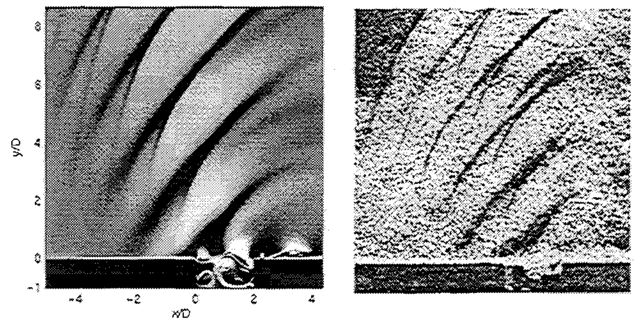

(a) (b)

Figure 4: Schlieren pictures corresponding to transversal derivative of the density: (a) present simulation, (b) Krishnamurty's experiment.[7]

Near-field results

The near-field is now investigated to try to identify the noise generation mechanism, and in particular to determine the origin of the two waves patterns noted previously. Figure 5 presents the vorticity field over one period of well-established self-sustained oscillations. In figure 5(a), the shear layer is seen to reattach at the trailing edge and two vortical structures can be identified in the shear layer. The first one is just shed from the leading edge separation. This rolled-up vortex travels downstream in the next pictures, growing with convection. The second structure is located just upstream of the downstream edge. As it impinges the edge (fig. 5(b)), the incident vortex is clipped at its centre. Part of the vortex spills over the cavity and is convected downstream, increasing the thickness of the reattached boundary layer. The other component is swept downwards into the cavity creating recirculating regions (fig. 5(c)). In figure 5(d), the vortex generated at the leading edge in the first picture arrives at the trailing edge, sustaining the vortex impingement process.

The corresponding time matched pressure field is depicted in figure 6. It is not easy to identify origins of noise generation because three different patterns are superposed. The first one is associated with the two coherent structures evolving in the shear layer. Low pressure regions in the shear layer identify vor-

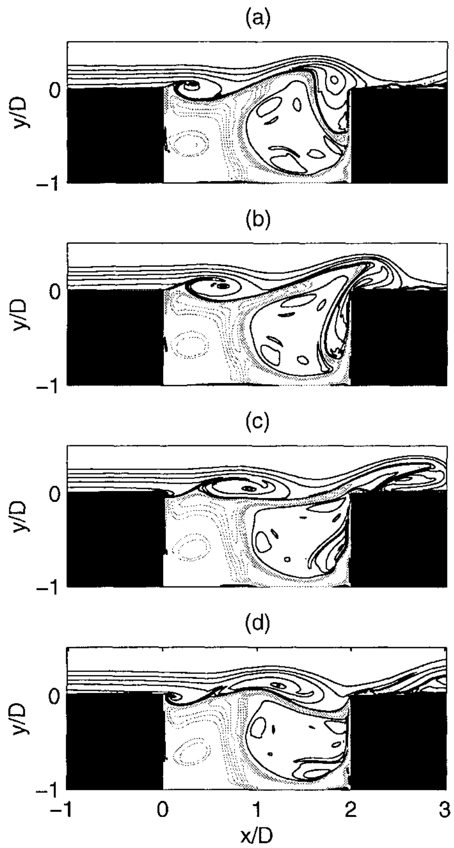

Figure 5: Instantaneous vorticity contours at four times during one cycle. 16 contours between $\omega D/U_\infty = -10.5$ and 1.36: (——) negative contours, (·······) positive contours. Zoom in and around the cavity.

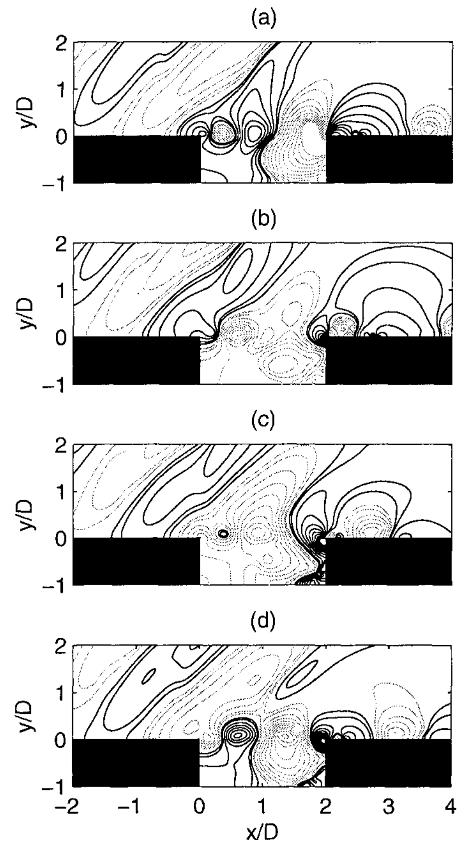

Figure 6: Instantaneous pressure contours at four times during one cycle. 22 contours between -10^4 and 10^4 Pa: (——) positive contours, (·······) negative contours. Zoom in and around the cavity.

tices, separated by high pressure regions. The two low-pressure centers are clearly visible in fig. 6(d). The first one is associated with the vortex roll-up at the leading edge. The second one corresponds to the second vortex convected by the flow before it impinges the upsteam edge. The second pressure pattern represents the recirculating flow in the cavity. As seen in the vorticity snapshots, a principal recirculation zone is located in the second half of the cavity, corresponding with the low pressure region inside the cavity, identifiable in fig. 6(b) et 6(c). This large-scale region is not a single vortex but is actually made up of several smaller vortices, arising from the clipping process, and its central region is vorticity free. Endly, the third group of pressure waves is the acoustic radiation generated by the flow. Figure 6 shows the birth of a positive pressure wave in the impingement process. The previously generated wave, located at the leading edge in fig. 6(a), escapes from the cavity in fig. 6(d). In the latter picture, the pressure wave seems to result from the superposition of two acoustic radiations. It is yet difficult to identify the two sources in the presence of interferences. This point will be discuss again in the next part.

3. Validation of integral methods

3.1 Introduction

In the present simulation, the acoustic part of the mesh represents more than the half of the total number of grid points, corresponding only to 6 cavity depths. In order to ensure the six points per wavelength required by Tam & Webb's stencil for the smallest acoustic wavelength present in the computational domain (occuring here when a direct acoustic ray interfers with the reflected one), we have an acoustic cut-off Strouhal number $\mathrm{St}_c = f_{min}L/U_\infty = L/(6\Delta y_{acous}\mathrm{M}_\infty) \simeq 21$. A reasonable calculation can then include only few wavelengths whereas realistic problems require observers at a distance of about two or three orders of magnitude greater than the cavity length. For these distances, it is certainly not discerning to perform a direct acoustic calculation.

The integral methods, instead, permit one to obtain the acoustic pressure at any points of the field, with a computational time independent of the observer distance. Typical calculations are carried out in two steps: an aerodynamic code based on CFD/CAA algorithms is used to evaluate the flow field, and then an integral formulation is applied to propagate the pressure disturbances in the farfield. Numerous integral methods are nowadays available. They rest upon two principal physical backgrounds: first, the acoustic analogies which split the computational domain in an aerodynamic region, where source terms responsible for noise generation are built up, from an acoustic region governed by a linear wave equation; second, the wave extrapolation methods which allow the evaluation of the far-field once some quantities are known on a control surface. From a physical point of view, it is important to notice that the extrapolation methods like Kirchhoff's formula are valid for any phenomena governed by the linear wave equation like optics, acoustics or electromagnetism while the acoustic analogy is based on the conservation laws of mass, momentum, and energy and is thus dedicated to aeroacoustics.

Recent advances in integral methods were essentially developed for the reduction of helicopter rotor noise[24] and have been recently applied for the prediction of jet noise.[25,26] Zhang, Rona, and Lilley[27] have used Curle's spatial formulation to obtain farfield spectra of cavity noise but no validation were proposed.

3.2 Acoustic analogy

The acoustic analogy was proposed by Lighthill[1] and was extended by Curle[28] and Ffowcs Williams and Hawkings[2] to include the effects of solid surfaces in arbitrary motion. The FW-H equation is an exact rearrangement of the continuity equation and Navier-Stokes equations into the form of an inhomogeneous wave equation with two surface source terms and a volume source term. The use of generalized functions to describe flow quantities permits one to embed the exterior flow problem in unbounded space. An integral solution can thus be obtained by convoluting the wave equation with the free-space Green function.

A serious restriction is that the observation region is assumed at rest. It is difficult to extend the propagation operator to include more complex flows. Only the case of a uniform flow is satisfactorily treated. Ffowcs Williams and Hawkings proposed the use of a Lagrangian coordinate transform assuming the surface is moving in a fluid at rest. Goldstein[29] preferred to take the convection effects in the wave equation. In the same manner, in the case of a motion with constant velocity $\mathbf{U}_\infty = (U_1, 0)$, the application of the Galilean transformation from the observer position $(\mathbf{x}, t)$ to $(\boldsymbol{\eta}, \bar{t})$,

$$\eta_i = x_i + U_i t, \quad \bar{t} = t$$

leads to the convected FW-H equation[30]:

$$\begin{aligned}&\left(\frac{\partial^2}{\partial \bar{t}^2} + U_i U_j \frac{\partial^2}{\partial \eta_i \eta_j} + 2U_i \frac{\partial^2}{\partial \eta_i \bar{t}}\right.\\ &\left.-c_\infty^2 \frac{\partial^2}{\partial \eta_i^2}\right) \left(H(f) c_\infty^2 \rho'(\boldsymbol{\eta}, \omega)\right)\\ &\quad = \frac{\partial^2}{\partial \eta_i \partial \eta_j} \left(\tilde{T}_{ij}(\boldsymbol{\eta}, \omega) H(f)\right)\\ &\quad - \frac{\partial}{\partial \eta_i} \left(\tilde{F}_i(\boldsymbol{\eta}, \omega)\delta(f)\right) + \frac{\partial}{\partial \bar{t}} \left(\tilde{Q}(\boldsymbol{\eta}, \omega)\delta(f)\right) \qquad (1)\end{aligned}$$

where the modified source terms including convection can be written as:

$$\tilde{T}_{ij} = \rho(u_i - U_i)(u_j - U_j) + \left[p - c_\infty^2 \rho'\right] \delta_{ij} - \tau_{ij} \qquad (2)$$

$$\tilde{F}_i = \left[\rho_\infty U_i U_j + p\delta_{ij} - \tau_{ij}\right] \frac{\partial f}{\partial \eta_j} \qquad (3)$$

$$\tilde{Q} = \left[-\rho_\infty U_j\right] \frac{\partial f}{\partial \eta_j} \qquad (4)$$

H is the Heaviside function and the function $f = 0$ defines the surface Σ outside of which the density field is calculated. f is scaled so that $\partial f / \partial \eta_j = \hat{n}_j$, the j-component of the unit normal vector pointing toward the interior of Σ. For a rigid body, we have simplified the surface source terms using the non-penetrating condition $u_n = \mathbf{u}.\hat{\mathbf{n}} = 0$.

For bidimensional geometries, it is more convenient to resolve this equation in the spectral domain.[30] The frequency domain formulation avoids the evaluation of the retarded time in three-dimensional problem, which can be a critical point. The gain over the time-domain applications is enhanced in 2-D because of the weaker properties of the Heaviside function which replaces the Dirac function in 2-D Green functions. Whereas the Dirac leads to a retarded time expression removing the temporal integration, the Heaviside function can only change the upper limit of the integration to a finite value, the lower limit remaining infinite. The spectral formulation removes this time constraint by solving FW-H equation harmonically. With application of the Fourier transform

$$\mathcal{F}\left[\phi(\mathbf{x}, t)\right] = \phi(\mathbf{x}, \omega) = \int_{-\infty}^{\infty} \phi(\mathbf{x}, t) e^{-i\omega t}\, dt \qquad (5)$$

equation (1) becomes

$$\left(\frac{\partial^2}{\partial \eta_i^2} + k^2 - 2iM_i k\frac{\partial}{\partial \eta_i} - M_iM_j\frac{\partial^2}{\partial \eta_i \partial \eta_j}\right)\left(H(f)c_\infty^2\rho'(\boldsymbol{\eta},\omega)\right) = -\frac{\partial^2}{\partial \eta_i \partial \eta_j}\left(\tilde{T}_{ij}(\boldsymbol{\eta},\omega)H(f)\right) + \frac{\partial}{\partial \eta_i}\left(\tilde{F}_i(\boldsymbol{\eta},\omega)\delta(f)\right) - i\omega\tilde{Q}(\boldsymbol{\eta},\omega)\delta(f) \qquad (6)$$

where $\mathrm{M}_i = U_i/c_\infty$. A Green function for this inhomogeneous convected wave equation is obtained from a Prandtl-Glauert transformation of the 2-D free-space Green's fonction in the frequency domain:

$$G(\boldsymbol{\eta} \mid \mathbf{y},\omega) = \frac{i}{4\beta}e^{i(\mathrm{M}k(\eta_1-y_1)/\beta^2)}H_0^{(2)}\left(\frac{kr}{\beta^2}\right)$$

where $r^2 = (\eta_1 - y_1)^2 + \beta^2(\eta_2 - y_2)^2$, $H_0^{(2)}$ is the Hankel function of the second kind and order zero, and $\beta = \sqrt{1-\mathrm{M}^2}$ is the Prandtl-Glauert factor, M< 1. The integral solution of equation (6) is then given by:

$$H(f)c_\infty^2\rho'(\boldsymbol{\eta},\omega) = -\int_{f=0}\tilde{F}_i(\mathbf{y},\omega)\frac{\partial G(\boldsymbol{\eta}\mid\mathbf{y})}{\partial y_i}\,d\Sigma - \int_{f=0} i\omega\tilde{Q}(\mathbf{y},\omega)G(\boldsymbol{\eta}\mid\mathbf{y})\,d\Sigma - \iint_{f>0}\tilde{T}_{ij}(\mathbf{y},\omega)\frac{\partial^2 G(\boldsymbol{\eta}\mid\mathbf{y})}{\partial y_i \partial y_j}\,d\mathbf{y} \qquad (7)$$

In 2-D, the volume integral is restricted to the surface $S_0(f>0)$ including the aerodynamic sources T_{ij} and the surface integrals are calculated on the solid lines which represent rigid boundaries. We applied the spatial derivatives on the Green function to avoid the evaluation of derivatives of aerodynamic quantities. It is formally equivalent to the transformation in temporal derivatives as performed by DiFrancescantonio[31] or Farassat and Myers.[32]

3.3 Wave extrapolation method

This kind of methods permits one to solve linear wave propagation problem once some flow quantities are given on a closed fictitious surface surrounding all the sources. The most famous one is the Kirchhoff's method which makes a parallel with electromagnetism by using Kirchhoff's formula. The main advantage with respect to acoustic analogy approaches is that only surface integrals have to be evaluated because all non linear quadrupolar sources are enclosed in the control surface. The problem is thus reduced by one dimension, which is particularly interesting in a numerical point of view. However, this approach suffers from the restriction that Kirchhoff's surface must strictly be in the linear acoustic region. Brentner and Farassat[33] and Singer[34] *et al.* show some misleading results when Kirchhoff's formulation is applied respectively to a hovering rotor blade and to the flow past a circular cylinder by using a control surface too close to the sources or crossing a shear layer.

A very clear analysis given by Brentner[24] shows that a wave extrapolation method based on the FW-H equation is relatively unaffected by the placement of the integration surface unlike Kirchhoff's formulation. We note FW-H WEM the Wave Extrapolation Method based on the FW-H formulation (7) by neglecting the volume integration (quadrupole source term $\tilde{T}_{ij}$). This FW-H WEM can combine the flexibility of the Kirchhoff's method and the physical insights of the FW-H equation.

FW-H and Kirchhoff formulations solve the same physical problem, the differences between the two writings being due to some choices made in the derivation process. In particular, the volume term of the Kirchhoff's formula include strictly all nonlinear aspects whereas a part of these aspects is moved in the dipole and monopole surface integrals in FW-H formulation. As a result, the two formulations work well when the control surface is in the far-field region but if it lies in a not-fully linear region, the Kirchhoff's results are erroneous and the FW-H WEM is more efficient. This method is sometimes called porous FW-H because it coincides with the application of FW-H analogy on a fictitious porous surface. The analytical developments are the same that those of FW-H analogy but the non-penetration condition $u_n = 0$ is no more required, and, in order to obtain correct results, one has to allow a fluid flow across Σ.

For a two-dimensional problem with uniform subsonic motion, FW-H WEM is given by equation (7) without the volume integral:

$$H(f)c_\infty^2\rho'(\boldsymbol{\eta},\omega) = -\int_{f=0}\tilde{F}_i(\mathbf{y},\omega)\frac{\partial G(\boldsymbol{\eta}\mid\mathbf{y})}{\partial y_i}\,d\Sigma - \int_{f=0} i\omega\tilde{Q}(\mathbf{y},\omega)G(\boldsymbol{\eta}\mid\mathbf{y})\,d\Sigma \qquad (8)$$

with the two source terms:

$$\tilde{F}_i = \left[\rho(u_i - 2U_i)u_j + \rho_\infty U_iU_j + p\delta_{ij} - \tau_{ij}\right]\frac{\partial f}{\partial x_j} \qquad (9)$$

$$\tilde{Q} = \left[\rho u_j - \rho_\infty U_j\right]\frac{\partial f}{\partial x_j} \qquad (10)$$

3.4 Numerical implementation

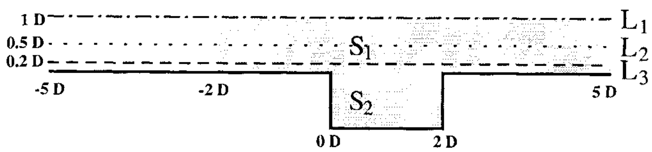

Figure 7: Schematic of the different line and surface sources for evaluation of integral formulations.

The fact that the FW-H equation can be the basis for either an acoustic analogy or a wave extrapolation method permits us to develop a single code. The choice of the method is made by neglecting the volume integral or imposing the non-penetration condition.

From an algorithmic point of view, there is almost no difference between the two approaches considered here. The first step is the recording of the aerodynamic quantities during one period of the DNS computation, using the pseudoperiodic behaviour of the oscillations in the cavity. The acoustic time step is 40 times the DNS time step corresponding to 131 points per wavelength. The variables (u_1, u_2, p, ρ) are recorded on three fictitious lines of the meshgrid for wave extrapolation method, and on the walls of the cavity and the surface around it for the acoustic analogy application as reported in figure 7.

Then the source terms are calculated and transformed in the frequency-domain using the Fourier transform defined by (5) for the positive frequencies. The contribution of the negative counterpart is equal and can be taken in account by doubling the final result. The integrals are then evaluated for each point of an acoustic meshgrid. This regular cartesian grid of 176×184 points covers a area of $(-5D; 5D) \times (-1D; 8D)$, corresponding with the main part of acoustic domain of DNS. Endly, an inverse Fourier transform is used to recover the acoustic signal in time-domain.

3.5 Results of porous FW-H

The extrapolation is performed from three lines spanning the longitudinal direction, of 501 points. The first line L_1 is chosen in the acoustic region at $y = 1D$ where a Kirchhoff's method would also have been applied. The second line L_2 is in the nearfied region at $y = 0.5D$, and the third line L_3 is still closer to the shear at $y = 0.2D$. The results of integration over L_1, L_2, and L_3 with source terms defined by (9), and (10), and with $M_\infty = 0.7$ in the observer domain are compared in figure 8. The three pressure fields obtained are consistent with the DNS. The contour plots are sharper when the surface is farther from sources. This is confirmed by the pressure profile of figure 9, and by the overall sound pressure directivity of figure 10. The three profiles predicted by the FW-H WEM are in good agreement with the DNS result. The small differences could be attributed to the fact that not all of the quadrupolar sources are taken into account when the integration surface is too close to the walls.

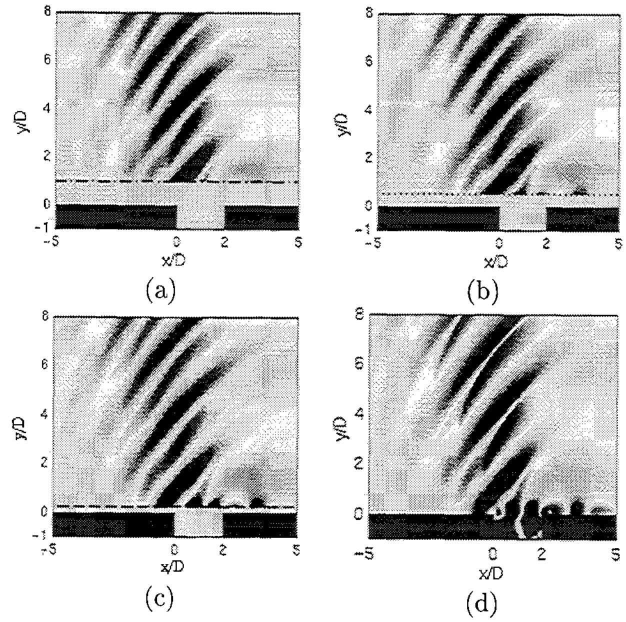

Figure 8: Pressure field calculated at the same time by (a) FW-H WEM from L_1, (b) FW-H WEM from L_2, (c) FW-H WEM from L_3, (d) DNS.

3.6 Results of FW-H analogy

When we apply FW-H analogy, the surface integrals are evaluated on the physical rigid walls of the cavity (solid lines of figure 7). The good results of porous FW-H method on L_3 placed at $y = 0.2D$ indicates that the volume sources above this line would be negligible. In the present evaluation, the chosen volumes are depicted in figure 7: S_2 is the surface inside the cavity, and S_1 the surface above it. S_1 is $1D$ high, and extends from $-2D$ to $5D$ in streamwise direction. However, the evaluation of volume integrals of T_{ij} are sensible to truncature effets, especially in the streamwise direction where the source terms decrease slowly. It is due to the presence of advected vortices, ejected from the cavity during the

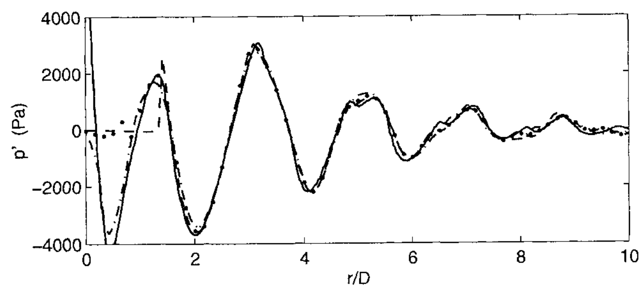

Figure 9: Pressure profile along the line x-2D=-y obtained by: (— · — ·) FW-H WEM from L_1, (· · · · · ·) FW-H WEM from L_2, (— — —) FW-H WEM from L_3, (——) DNS. $r = \sqrt{x^2 + y^2}$

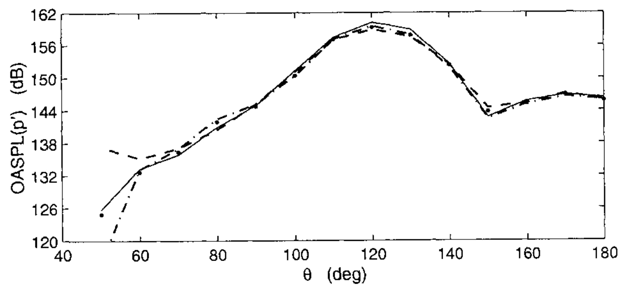

Figure 10: Overall sound pressure level as function of θ measured from streamwise axis, evaluated on the sensors reported in figure 1. Same legend as fig. 9

clipping process, in the reattached boundary layer on the downstream wall.

To obtain the volume integral part of the radiated sound field, we add the contributions of S_1 and S_2 (figure 11(a)). The surface integration is performed on cavity walls with source terms defined by (3) and (4), with $M_\infty = 0.7$. The result is depicted in figure 11(b). Following reflection theorem of Powell,[35] we can argue that volume integrals represent the direct radiated field, and surface integrals show essentially the reflected part of the field due to cavity walls. By summing the volume and surface contributions (fig. 12(a)), we reconstruct the total sound field in reasonably good agreement with the DNS reference solution of figure 12(b). Figure 13 shows that the pressure profile along the line $x + y = 2D$ is consistent with direct calculation.

Figure 14 presents the temporal evolutions of the pressure over one period using the three methods. DNS results show a very stiff slope for the temporal evolution, which indicates a non-linear propagation. The two integral formulations time traces have a sinusoidal shape. The non-linear effects are indeed not taken into account in integral methods since the

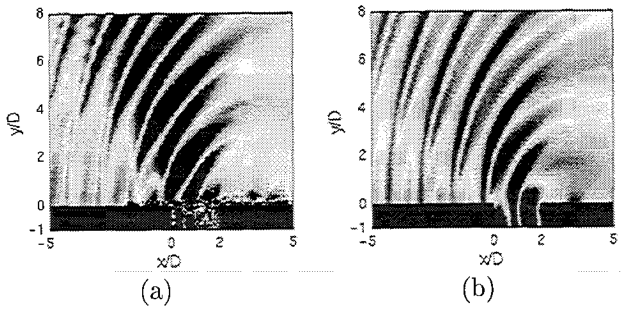

Figure 11: Pressure field obtained corresponding to: (a) volume integral part of FW-H analogy, and (b) surface integral part of FW-H analogy.

volume integral is neglected in FW-H WEM and the volume integral does not include all the non-linear region in FW-H analogy.

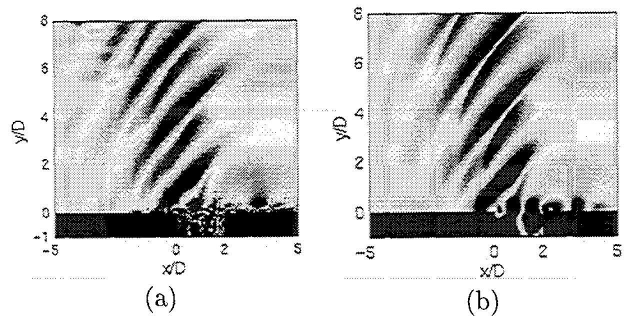

Figure 12: Pressure field calculated at the same time by (a) FW-H analogy (surface + volume integrals), (b) DNS reference solution.

The FW-H analogy provides more informations than the WEM but is more expensive in CPU time because of the evaluation of volume integral (surface integral in 2-D) whereas wave extrapolation methods need only surface integral (line integral in 2-D). For example, the computation time needed by the FW-H WEM is around 13 minutes, whereas the FW-H analogy requires 17 hours, on a Dec α computer. For the purpose of comparison, the DNS would take 320 hours on this machine.

FW-H analogy allows a better understanding of the structure of the radiated field than WEM. In particular, the direct and reflected sound field can be separated. These two fields at the same frequency give an interference figure where the two waves patterns are still distinguishable in our case because the cavity is not compact at the oscillation frequency ($L/\lambda = 0.47$).

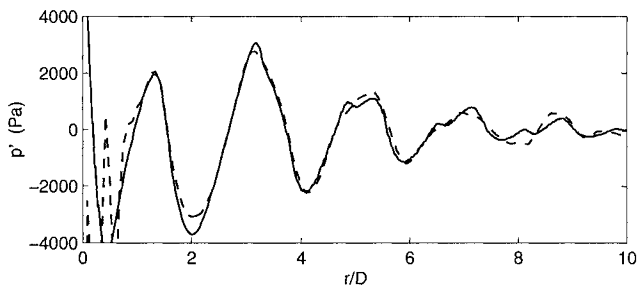

Figure 13: Pressure profile along the line x-2D=-y obtained by: (— — —) FW-H analogy, (——) DNS.

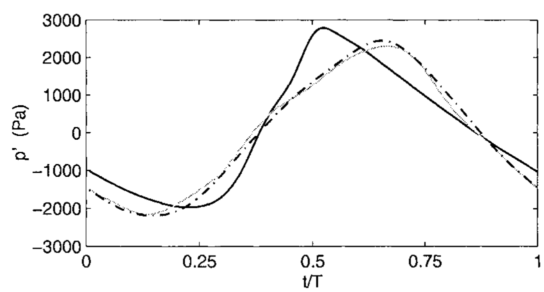

Figure 14: Time traces of fluctuating pressure over an oscillation period T at the point $x/D = -1.28$ and $y/D = 6.14$: (——) DNS, (— · — ·) FW-H WEM from L_1, (·········) FW-H analogy. $r = \sqrt{x^2 + y^2}$

5. Conclusion

In a first part, a direct calculation of the sound radiated by a flow over a 2-D rectangular cavity is carried out. To this end, a DNS is performed using CAA numerical methods. This approach is expensive but is able to give all the interactions between flow and acoustics and provides a powerful tool to determine noise generation mechanisms. The directly computed sound field is consistent with corresponding results of Krishnamurty's experiments.

The results of DNS are then successfully compared to two hybrid methods which use the DNS aerodynamic quantities to solve integral formulations based on FW-H equation. The wave extrapolation method using FW-H equation is relatively unaffected by the location of the control surface and can be an interesting complementary tool to extend CAA near-field to the very far-field. Acoustic analogy is less efficient because volume integrations are costly and sensible to truncature effects. Nevertheless, it allows a separation between direct and reflected sound fields, which is usefull for the analysis of radiation patterns.

For a finer analysis, a 3-D simulation should be carried out. The recirculation zone inside the cavity is indeed characterized by a three-dimensional turbulent mixing, even if the development of the shear layer is almost two-dimensional. Such a study is underway.

Acknowledgments

Computing time is supplied by Institut du Développement et des Ressources en Informatique Scientifique (IDRIS - CNRS).

References

[1] Lighthill, M.J., 1952, On sound generated aerodynamically I. General theory, *Proc. of the Royal Society of London*, **A 211**, p. 564–587.

[2] Ffowcs Williams, J.E. & Hawkings, D.L., 1969, Sound generated by turbulence and surfaces in arbitrary motion, *Philosophical Transactions of the Royal Society*, **A264**(1151), p. 321–342.

[3] Freund, J.B., Lele, S.K. & Moin, P., 1993, Matching of near/far-field equation sets for direct computations of aerodynamic sound, *AIAA Paper 93-4326.*

[4] Bailly, C., Bogey, C. & Juvé, D., 2000, Computation of flow noise using source terms in linearized Euler's equations, *AIAA Paper 2000-2047.*

[5] Bogey, C., Bailly, C. & Juvé, D., 2000, Computation of the sound radiated by a 3-D jet using large eddy simulation, *AIAA Paper 2000-2009.*

[6] Rockwell, D., 1983, Oscillations of impinging shear layers, *AIAA Journal*, **21**(5), p. 645–664.

[7] Krishnamurty, K. Acoustic radiation from two-dimensional rectangular cutouts in aerodynamic surfaces. *Tech. Note* 3487, N.A.C.A., 1955.

[8] Hankey, W.L. & Shang, J.S., 1980, Analyses of pressure oscillations in an open cavity, *AIAA Journal*, **18**(8), p. 892–898.

[9] Slimon, S.A., Davis, D.W. & Wagner, C.A., 1998, Far-field aeroacoustic computation of unsteady cavity flow, *36th Aerospace Science Meeting & Exhibition, AIAA 98-0285.*

[10] Tam, C.-J., Orkwis, P.D. & Disimile, P.J., 1995, Comparison of Baldwin-Lomax turbulence models for two-dimensional open cavity computations, *AIAA Journal*, **34**(3), p. 629–631.

[11] Rona, A. & Dieudonné, W., 2000, A flow-resonant model of transonic laminar open cavity instability, *AIAA Paper 2000-1967.*

[12] Zhang, X., 1995, Compressible cavity flow oscillation due to shear layer instabilities and pressure feedback, *AIAA Journal*, **33**(8), p. 1404–1411.

[13] COLONIUS, T., BASU, A.J. & ROWLEY, C.W., 1999, Numerical investigation of the flow past a cavity, *AIAA Paper 99-1912.*

[14] SHIEH, C.M. & MORRIS, P.J., 1999, Parallel numerical simulation of subsonic cavity noise, *AIAA Paper 99-1891.*

[15] GHARIB, M. & ROSHKO, A., 1987, The effect of flow oscillations on cavity drag, *J. Fluid Mech.*, **177**, p. 501–530.

[16] GLOERFELT, X., BAILLY, C. & JUVÉ, D., 2000, Calcul direct du rayonnement acoustique d'un écoulement affleurant une cavité, *C. R. Acad. Sci., t.* **328**, *Série IIb.*

[17] SHIEH, C.M. & MORRIS, P.J., 2000, Parallel computational aeroacoustic simulation of turbulent subsonic cavity flow, *AIAA Paper 2000-1914.*

[18] NAJM, H.N. & GHONIEM, A.F., 1991, Numerical simulation of the convective instability in a dump combustor, *AIAA Journal*, **29**(6), p. 911–919.

[19] BOGEY, C. *Calcul direct du bruit aérodynamique et validation de modèles acoustiques hybrides.* PhD thesis, Ecole Centrale de Lyon, 2000. No 2000-11.

[20] TAM, C.K.W. & WEBB, J.C., 1993, Dispersion-relation-preserving finite difference schemes for computational acoustics, *J. Comput. Phys.*, **107**, p. 262–281.

[21] TAM, C.K.W. & DONG, Z., 1996, Radiation and outflow boundary conditions for direct computation of acoustic and flow disturbances in a nonuniform mean flow, *J. Comput. Acous.*, **4**(2), p. 175–201.

[22] BOGEY, C., BAILLY, C. & JUVÉ, D., 2000, Numerical simulation of sound generated by vortex pairing in a mixing layer, *AIAA Journal*, **38**(12), p. 2210–2218.

[23] ROSSITER, J.E. Wind-tunnel experiments on the flow over rectangular cavities at subsonic and transonic speeds. Technical Report 3438, Aeronautical Research Council Reports and Memoranda, 1964.

[24] BRENTNER, K.S., 2000, Modeling aerodynamically generated sound: Recent advances in rotor noise prediction, *AIAA Paper 2000-0345.*

[25] COLONIUS, T. & FREUND, J.B., 2000, Application of Lighthill equation to a Mach 1.92 turbulent jet, *AIAA Journal*, **38**(2), p. 368–370.

[26] BOGEY, C., BAILLY, C. & JUVÉ, D., 2001, Noise computation using Lighthill's equation with inclusion of mean flow - acoustics interactions, *AIAA Paper 2001-2255.*

[27] ZHANG, X., RONA, A. & LILLEY, G.M., 1995, Far-field noise radiation from an unsteady supersonic cavity, *AIAA Paper 95-040.*

[28] CURLE, N., 1955, The influence of solid boundaries upon aerodynamic sound, *Proc. of the Royal Society of London*, **A 231**, p. 505–514.

[29] GOLDSTEIN, M.E., 1976, *Aeroacoustics*, McGraw-Hill, New York.

[30] LOCKARD, D.P., 2000, An efficient, two-dimensional implementation of the Ffowcs Williams and Hawkings equation, *J. Sound Vib.*, **229**(4), p. 897–911.

[31] DI FRANCESCANTONIO, P., 1997, A new boundary integral formulation for the prediction of sound radiation, *J. Sound Vib.*, **202**(4), p. 491–509.

[32] FARASSAT, F. & MYERS, M.K., 1988, Extension of Kirchhoff's formula to radiation from moving surfaces, *J. Sound Vib.*, **123**(3), p. 451–460.

[33] BRENTNER, K.S. & FARASSAT, F., 1998, An analytical comparison of the acoustic analogy and Kirchhoff formulation for moving surfaces, *AIAA Journal*, **36**(8), p. 1379–1386.

[34] SINGER, B.A., BRENTNER, K.S., LOCKARD, D.P. & LILLEY, G.M., 2000, Simulation of acoustic scattering from a trailing edge, *J. Sound Vib.*, **230**(3), p. 541–560.

[35] POWELL, A., 1960, Aerodynamic noise and the plane boundary, *J. Acoust. Soc. Am.*, **32**(8), p. 982–990.